Journal of Catalysis **187,** 177–185 (1999)
Article ID jcat.1999.2589, available online at http://www.idealibrary.com on IDEAL®

Relationships between Structural/Textural Properties and Redox Behavior in $Ce_{0.6}Zr_{0.4}O_2$ Mixed Oxides

Paolo Fornasiero, Emiliano Fonda, Roberta Di Monte, Gilberto Vlaic, Jan Kašpar,[1] and Mauro Graziani

Dipartimento di Scienze Chimiche, Università di Trieste, 34127 Trieste, Italy

Received March 29, 1999; revised June 4, 1999; accepted June 4, 1999

The redox behavior and the structural properties of $Ce_{0.6}Zr_{0.4}O_2$ mixed oxides of high surface area and dense ceramic-type materials are compared. It is shown that due to the insertion of ZrO_2 into the CeO_2 lattice the oxygen sublattice becomes significantly distorted: Zr–O coordination of the type $5+2$ and $4+2$ is found in the former and latter samples, respectively. The nature of these distortions is correlated with the origin of the sample and it appears also to be related to the particle size of the $Ce_{0.6}Zr_{0.4}O_2$ mixed oxide. Noticeably, the reduction behavior of these samples as investigated by the temperature-programmed reduction method appears correlated with their structural properties. © 1999 Academic Press

Key Words: **CeO_2–ZrO_2 mixed oxides, redox property of; CeO_2–ZrO_2 solid solution; local structure; oxygen storage capacity; three-way catalysts; Rh/CeO_2–ZrO_2 mixed oxides, Raman and EXAFS characterization of.**

1. INTRODUCTION

Recently, there has been a strong interest in the investigation of redox properties of CeO_2–ZrO_2 mixed oxides due to their extensive use as promoters for three-way catalysts (TWCs). Due to their high thermal stability and enhanced redox properties compared to the traditionally employed CeO_2, these systems are now employed as a so-called oxygen storage device (1, 2). Oxygen storage and release capacity (OSC) is the ability of a TWC to store oxygen under net oxidizing conditions and release it under net reducing conditions, thereby maintaining the air-to-fuel ratio at close to stoichiometric conditions, where the highest conversions are attained.

We have extensively investigated the CeO_2–ZrO_2 mixed oxides, both noble metal-loaded and metal-free, and showed that structural and textural factors play an important role in determining the reduction behavior and hence OSC (2, 3). This is due to the fact that when the redox properties are investigated by means of the temperature-programmed reduction method, the reduction behavior seems related to the mobility of the oxygen in the bulk of the mixed oxide. This has recently been confirmed also by isotopic studies (4). As recently shown for highly sintered CeO_2–ZrO_2 mixed oxides, a remarkable property is that insertion of ZrO_2 into the CeO_2 lattice distorts the oxygen sublattice, making mobile lattice oxygen available for redox processes (5). At comparable textural properties, e.g., ceramic-type samples, the nature of these distortions depends on ZrO_2 content (6). In fact, dependency of redox/structural properties has been reported for $Ce_{0.5}Zr_{0.5}O_2$ (3). Here we investigate how these oxygen sublattice modifications are related to the texture and the origin of the $Ce_{0.6}Zr_{0.4}O_2$ mixed oxide. This composition was preferred here with respect to previously investigated $Ce_{0.5}Zr_{0.5}O_2$ because for this sample, transition between the tetragonal and the cubic phases easily occurs, according to the synthesis method/pretreatment (2). Temperature-programmed reduction, N_2 physisorption, and Raman and EXAFS techniques are applied to analyze the relationships among the textural, structural, and redox properties.

2. EXPERIMENTAL PROCEDURES

The low-surface-area (LSA) $Ce_{0.6}Zr_{0.4}O_2$ was from a previous study (2, 7). It was prepared by solid state synthesis, by firing mixtures of the oxides at 1873 K for 1 h. This support was loaded with $RhCl_3$ as metal precursor. Rh nominal loading was 0.5 wt%. The high-surface-area (HSA) $Ce_{0.6}Zr_{0.4}O_2$ was prepared by a citrate route as recently described (8), using water as solvent. The recycled (REC) $Ce_{0.6}Zr_{0.4}O_2$ was prepared from the HSA $Ce_{0.6}Zr_{0.4}O_2$ by running a temperature-programmed reduction (see below) up to 1273 K, followed by an *in situ* reoxidation at 700 K.

Temperature-programmed reduction (TPR) experiments were carried out as previously described (2). Oxygen uptake was measured at 700 K by a pulse method (2).

EXAFS spectra of Zr K-edge of standard and catalytic samples were collected at LURE on beamline EXAFS I using a Si (331) channel cut monochromator. Detectors were two ionization chambers filled with Ar at atmospheric pressure. All samples were crushed in a mortar to obtain a fine

[1] To whom correspondence should be addressed. Fax: +39-040-6763903. E-mail: kaspar@univ.trieste.it.

0021-9517/99 $30.00

powder and then pressed at 7.6×10^8 N m^{-2} to obtain self-supporting pellets. Weights of samples were calculated to obtain a 2.5 total absorption coefficient. Zirconium K-edge spectra had been collected at room temperature (RT) in the energy interval 17.9–18.9 keV with a 2-eV step and a 2-s integration time. $BaZrO_3$ was used as a reference for the Zr–O scattering pair, using the following structural parameters to obtain phases and amplitudes: $N = 6$, $R = 2.095$ Å, $\sigma = 0.07$ Å.

EXAFS spectra of Ce L_{III}-edge of standard (CeO_2) and catalytic samples were collected on the same beamline as the Zr K-edge spectra. The ionization chambers were filled with air at atmospheric pressure. The data were recorded at RT with a 2-eV step from 5680 to 6190 eV and a 2-s integration time. LSA $Ce_{0.6}Zr_{0.4}O_2$ was prepared by mixing the powder with boron nitride in a mortar and then pressed at 7.6×10^8 N m^{-2}. A weight ratio sample/boron nitride equal to 1/4.5 was employed. HSA $Ce_{0.6}Zr_{0.4}O_2$ and REC $Ce_{0.6}Zr_{0.4}O_2$ were deposited on a millipore membrane from a cyclohexane suspension. Weights of samples were calculated to obtain a 2.5 total absorption coefficient. CeO_2 as a pelletized CeO_2/boron nitride mixture and CeO_2 deposited on a membrane were employed as standards. The following structural parameters were used to obtain phases and amplitudes: $N = 8$, $R = 2.341$ Å, $\sigma = 0.07$ Å.

Due to the unavailability of Ce–Zr standards, we calculated *ab initio* scattering phases, amplitudes, and mean free path using the FEFF7.0 code (9). A CeO_2 lattice with 40% of Ce positions being replaced by Zr was used as a model. The cell parameter was chosen to be equal to that found by XRD for the LSA sample.

Powder XRD spectra were collected on a Siemens Kristalloflex Mod.F Instrument (Ni-filtered CuK_α). Cell parameters were determined from the XRD patterns using the TREOR90 program. The profile fitting of the XRD patterns was performed by a Rietveld analysis program (RIETAN94). The peak shape was assumed to be a modified pseudo-Voigt function with asymmetry. The background of each profile was approximated by a nine-parameter polynomial in $2\theta^m$. FT-Raman spectra were measured on a Perkin–Elmer 2000 FT-Raman with a diode pumped YAG laser and a RT super InGaAs detector. The laser power was 50–400 mW.

3. RESULTS AND DISCUSSION

3.1. Textural Characterization and Redox Behavior

Results of textural characterization by N_2 physisorption are reported in Table 1. Negligible surface areas and no appreciable porosity are detected on the LSA sample, indicating that any redox activity of this sample must be associated with processes occurring in the bulk of the mixed oxide. In contrast, the HSA sample features a surface area of 50 m^2 g^{-1}, which decreases to 2 m^2 g^{-1} upon redox cycling as described under Experimental Procedures. Even if the surface area of the REC $Ce_{0.6}Zr_{0.4}O_2$ collapsed to a rather small value, it is significantly higher than that of the LSA samples. Moreover, the latter sample conserves some residual mesoporosity, which is induced by the expansion/contraction of the lattice parameter in the redox cycles (3).

TABLE 1

Textural Characterization of the $Ce_{0.6}Zr_{0.4}O_2$ Mixed Oxides by Means of Volumetric N_2 Physisorption at 77 K

Sample	BET surface area (m^2 g^{-1})	Pore volume[a] (μl g^{-1})	Average pore radius[a] (nm)
LSA $Ce_{0.6}Zr_{0.4}O_2$	<1	—	—
HSA $Ce_{0.6}Zr_{0.4}O_2$	50	27	4
REC $Ce_{0.6}Zr_{0.4}O_2$	2	5	60

[a] Calculated by the BJH method from the desorption isotherm.

The variation of the sample texture strongly affects the redox behavior as depicted by the TPR profiles reported in Fig. 1. In fact, almost no reduction is observed at low

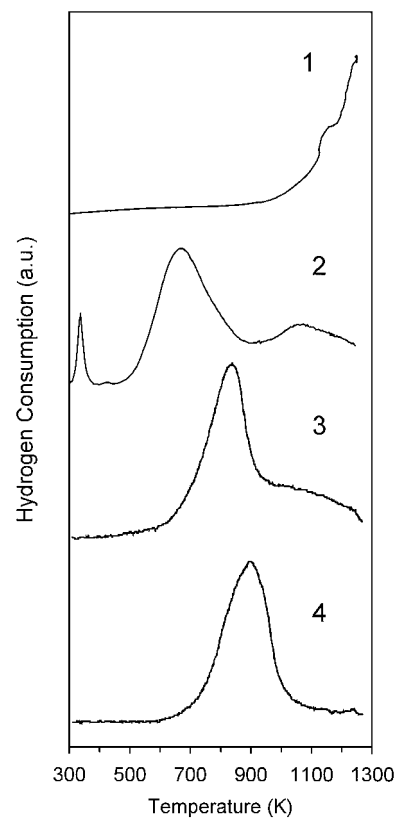

FIG. 1. Temperature-programmed reduction profiles of LSA $Ce_{0.6}Zr_{0.4}O_2$ (1), LSA Rh/$Ce_{0.6}Zr_{0.4}O_2$ (2), HSA $Ce_{0.6}Zr_{0.4}O_2$ (3), and REC $Ce_{0.6}Zr_{0.4}O_2$ (4).

temperatures in the LSA $Ce_{0.6}Zr_{0.4}O_2$. This is due to the negligible surface area and the high-temperature treatment, which makes almost no surface hydroxyls available for H_2 activation. Accordingly, on this sample the reduction process is limited by the difficulty of H_2 activation at the surface (7). When rhodium is added to this sample, H_2 activation becomes easy and a strong reduction feature is observed at 700 K, which is attributed to the reduction in the bulk of the mixed LSA $Ce_{0.6}Zr_{0.4}O_2$. In this case, the supported metal activates H_2, making diffusion of oxygen in the bulk the rate-determining step of the reduction. Due to the dense nature of this ceramic type of material, and the extremely low surface area, other kinds of interactions between the supported metal and the support itself, which could affect the appearance of the reduction process, are unreliable. In contrast such phenomena have been detected on HSA NM/$Ce_{0.5}Zr_{0.5}O_2$ (10, 11). Accordingly, we associate the differences in the reduction behavior of the LSA Rh-loaded, HSA and REC $Ce_{0.6}Zr_{0.4}O_2$ to different structural/textural properties of the mixed oxide. Notice that the following order reactivity is found: LSA Rh-loaded, HSA $Ce_{0.6}Zr_{0.4}O_2$, and REC $Ce_{0.6}Zr_{0.4}O_2$, as detected by the sequence of peak temperatures reported in Fig. 1. The degree of reduction after the TPR experiment was evaluated by measuring the O_2 uptake at 700 K. Oxygen uptakes of 8.4, 17.4, and 17.6 ml O_2 g^{-1} were measured for the LSA, HSA, and REC samples, respectively, which leads to final compositions of $Ce_{0.6}Zr_{0.4}O_{1.91}$ for the LSA sample and $Ce_{0.6}Zr_{0.4}O_{1.81}$ for HSA and REC samples.

3.2. Structural Characterization: XRD and Raman Results

Powder XRD patterns of the investigated samples are reported in Fig. 2. All the reported patterns can be conveniently indexed in the *Fm*3*m* space group, e.g., a fluorite-type of structure. Notice that this indexing is related to the cation sublattice, since contribution of the oxygen to the XRD patterns is small. Accordingly, Raman and EXAFS spectroscopies best reveal the distortions of the oxygen sublattice (5, 12). The lattice parameter and the calculated M–O bond lengths as calculated from the indexed spectra are reported in Table 2.

Noticeably, the cell parameter of the HSA sample is significantly higher than that of LSA sample. Redox cycling of the sample leads to a cell parameter that is close to that of the LSA sample. The high cell parameter of HSA $Ce_{0.6}Zr_{0.4}O_2$ is in line with a recent survey of the use of CeO_2–ZrO_2 in three-way catalysis, in which it was observed that according to the origin of the sample, e.g., ceramic type or "HSA type," different lattice parameters were observed

TABLE 2

Lattice Parameter, M–O Bond Lengths, and Particle Size as Detected from Powder XRD Patterns

Sample	Cell parameter[a] (Å)	M–O bond length[b] (Å)	Particle size (nm)
LSA	5.307 (1)	2.298	>90
HSA	5.321 (5)	2.304	6
HSA calcined at 1273 K	5.327 (1)	2.307	20
REC	5.306 (1)	2.298	19

[a] Standard deviation is given in parentheses. *Fm*3*m* symmetry is considered.

[b] The powder cell program written by W. Krause and G. Nobel, Fed.Inst.Mater.Res.Test, Berlin, Germany was employed to calculate the M–O bond lengths, using the parameters obtained from TREOR90 and assuming that oxygen atoms are located in the tetrahedral sites.

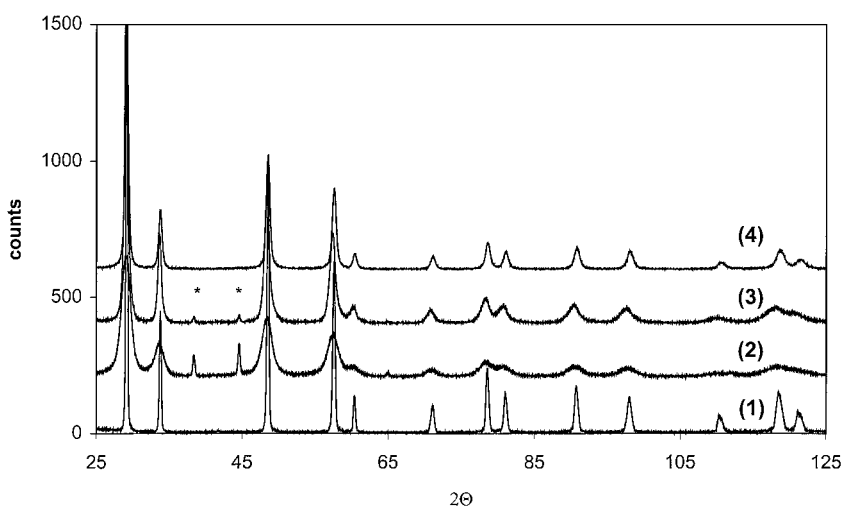

FIG. 2. Powder XRD patterns of LSA $Ce_{0.6}Zr_{0.4}O_2$ (1), HSA $Ce_{0.6}Zr_{0.4}O_2$ (2), HSA $Ce_{0.6}Zr_{0.4}O_2$ after calcination at 1273 K for 5 h (3), and REC $Ce_{0.6}Zr_{0.4}O_2$ (4). * Al holder.

in the literature (13). This suggested that the LSA and HSA CeO_2–ZrO_2 mixed oxides are structurally different.

Remarkable results were obtained for the HSA $Ce_{0.6}Zr_{0.4}O_2$ calcined at 1273 K for 5 h. In fact, the broadness of the XRD patterns of the fresh HSA $Ce_{0.6}Zr_{0.4}O_2$ does not allow one to unequivocally establish the presence of a solid solution. For this reason we calcined the HSA sample at 1273 K, which leads to significant sintering as detected by sharpening of all the reflections. By applying the Schrerrer formula we estimate that particle diameter increases from 6 to 20 nm. No evidence for phase separation is observed in this spectrum. Notice that thermal treatment cannot promote formation of a solid solution under these conditions. Due to the metastable nature of the CeO_2–ZrO_2 mixed oxides of intermediate composition (14), calcination of this sample should lead to a phase separation as detected on commercial samples of similar composition (15). Temperatures over 1473 K, where cation migration and Ce^{4+} reduction become significant, are necessary to obtain a homogeneous solid solution via solid state reaction (16). Therefore, this is a strong indication that by the present synthesis method a homogeneous HSA solid solution has been prepared.

The XRD pattern was profile fitted by using the Rietveld method (Table 3, Fig. 3). Both the *Fm*3*m* (cubic-fluorite type) and the $P4_2/nmc$ (tetragonal) symmetries were tested. As shown by the structural factors (R) reported in Table 3 and Fig. 3, spectrum 2, the XRD pattern of the HSA sample calcined at 1273 K can be conveniently fitted upon assumption of a *Fm*3*m* symmetry. However, it should be noted that the isotropic atomic thermal parameter (B) for the oxygen subshell is rather high if compared to 0.229–0.317 Å^2 typically found for doped zirconias (17). This is a strong indication of a high level of disorder in the oxygen sublattice. No evidence was found that the $P4_2/nmc$ model could fit the experimental data better than *Fm*3*m*. At variance, the $P4_2/nmc$ model fits the XRD profile of the LSA sample better than the *Fm*3*m* model, since more reliable R parameters are obtained (Table 3). Noticeably the $P4_2/nmc$ model gives a B parameter for oxygen, which is comparable to literature values. In contrast high values are obtained for the *Fm*3*m* model. However, as shown in Fig. 3, spectrum 1, there are systematic deviations in the difference spectra, suggesting inadequacy of the model. This is remarkable since the $P4_2/nmc$ symmetry has generally been proposed for samples of this composition (12, 18). Similar results were obtained for the *Fm*3*m* model (data not reported).

TABLE 3

Lattice Parameters and M–O Bond Lengths as Detected by the Profile Fitting of the Powder XRD Patterns Using the Rietveld Method

	HSA[a]	LSA	LSA
Symmetry	*Fm*3*m*	*Fm*3*m*	$P4_2/nmc$
a (nm)	0.53274(6)	0.530347(7)	0.374646(9)
c (nm)	0.53274(6)	0.530347(7)	0.53147(1)
V (nm^3)	0.15119	0.14917	0.14919
d (g/cm^3)	6.70	6.79	6.79
c/a	1	1	1.003
Cation x	0	0	0
Cation y	0	0	0
Cation z	0	0	0
B (Å^2)	0.38	0.40(8)	0.19(8)
O x	0.25	0.25	0
O y	0.25	0.25	0.5
O z	0.25	0.25	0.227
B (Å^2)	1.58(7)	2.29(8)	1.65(8)
R_{wp} (%)[b]	9.52	14.25	11.90
R_p (%)[c]	6.59	11.37	9.34
R_f (%)[d]	0.82	4.55	4.08
M—O	2.307	2.297	2.228 2.369

[a] Calcined at 1273 K for 5 h.
[b] R_{wp}, weighted pattern.
[c] R_p, pattern.
[d] R_f, structure factor.

Significant modifications of the M–O bonding compared to the ideal fluorite lattice are detected also by the Raman spectra (Fig. 4). The Raman spectrum of the HSA-$Ce_{0.6}Zr_{0.4}O_2$ features a strong broad band centered at 487 cm^{-1} with a shoulder at about 640 cm^{-1} and a weak band at 316 cm^{-1}. Six Raman-active modes of the $A_{1g} + 3\,E_g + 2\,B_{1g}$ symmetry are predicted for tetragonal ZrO_2 (space group $P4_2/nmc$), while for the space group *Fm*3*m* only one F_{2g} mode centered at around 490 cm^{-1} is Raman-active (19). The F_{2g} mode is observed at 465 cm^{-1} in CeO_2. The peak at 487 cm^{-1} would therefore be consistent with the presence of a "cubic" phase. A low-frequency tail of the Raman mode at 465 cm^{-1} was observed in CeO_2-trivalent rare earth mixed oxides and it was associated with the oxygen vacancies created upon Ce^{4+} substitution (20). The presence of the bands at 316 and 636 cm^{-1} is an indication of some distortion of the oxygen sublattice and it allows attribution to the t'' phase (12). This phase is characterized by a fluorite-type cation sublattice, while oxygen atoms were displaced from the ideal fluorite sites, giving a tetragonal phase (12). Noticeably, upon calcination at 1273 K, the intensity of the spectrum increases, which is consistent with an increase of crystal particle size (21), but no other appreciable modifications are seen. This suggests that the above-reported findings obtained by the Rietveld analysis can be directly related to the starting HSA sample.

The spectra of both REC and LSA $Ce_{0.6}Zr_{0.4}O_2$ appear strongly modified compared to that of HSA $Ce_{0.6}Zr_{0.4}O_2$. Seven bands at 179 (w), 314 (s), 453 (sh), 491 (s), 538 (s), 603 (s), and 647 (sh) are observed in the REC sample. Also the Raman pattern of the LSA sample features seven bands at 191 (br), 316 (s), 393 (s), 425 (vw), 480 (s), 521 (s), and 636 (s); however, significant differences are detected with

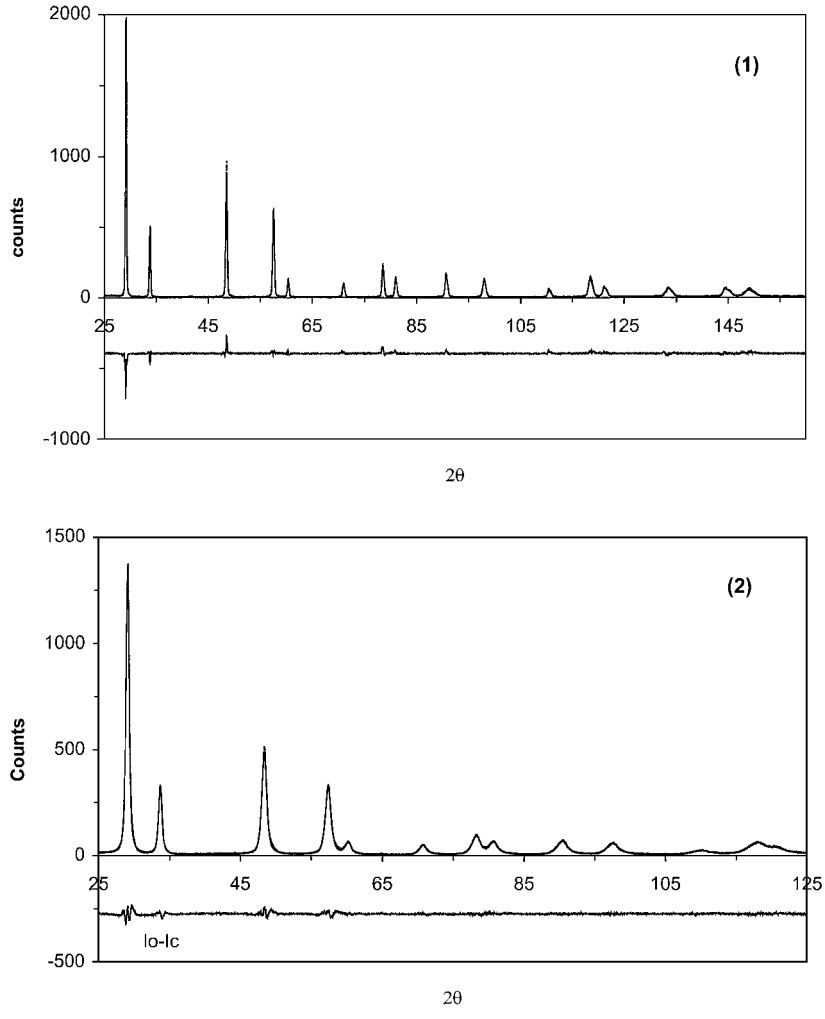

FIG. 3. Profile-fitting patterns of the LSA $Ce_{0.6}Zr_{0.4}O_2$ (1) using $P4_2/nmc$ symmetry and HSA $Ce_{0.6}Zr_{0.4}O_2$ calcined at 1273 K (2) using the $Fm3m$ symmetry: observed and calculated profile intensities and their differences ($I_o - I_c$) are reported on the same scale, including the $K\alpha_1$ and $K\alpha_2$ splitting. The calculated reliability factors are reported in Table 3.

respect to the REC sample. Notice, for example, the lack of a band at 393 cm^{-1} in REC $Ce_{0.6}Zr_{0.4}O_2$ and the different pattern/shift of the bands in the region 600–650 cm^{-1}. The exact symmetry of M–O cannot be detected for these two samples at this stage. In fact, bands in addition to those predicted by the symmetry rules were often found in the Raman spectra of doped zirconias. These bands were attributed to chemiluminescence and/or breakdown of the wave vector selection rules by translational disorder (12, 22). The ratio of intensities of the bands at 470–480 to 640 cm^{-1} has been employed to determine the cubic-to-tetragonal phase boundary, the latter band being claimed to be specific for tetragonal symmetry (22, 23). On the other hand, in the cubic CeO_2–ZrO_2 mixed oxides, the strong band at 470–480 cm^{-1} is associated with the F_{2g} Raman mode. In summary the Raman spectra clearly point out a strong decrease of the M–O bond symmetry in the REC and LSA samples, the local situation being different.

3.3. Structural Characterization: EXAFS Results

The analysis at the Zr K-edge was performed in two steps. First, we used the Fourier filtering method (24) and experimental standards to obtain accurate data on the first metal–oxygen shells of Zr and Ce (nearest neighbors, NN). We tested a large number of models with one, two, and three oxygen shells using the same procedure described in a previous paper (5). Each model was discriminated from other models on the basis of an F test. The results obtained by this procedure and which are physically meaningful are reported in Table 4. Due to the unavailability of the experimental standards for the Zr–Ce system, we performed the analysis of the next nearest neighbors (NNN) as follows. First, we fixed the coordination numbers obtained from the analysis of the first shell (Table 1). Then we analyzed the data by using the UWXAFS package over the whole range of shells, including NNN (25). Meaningful results were

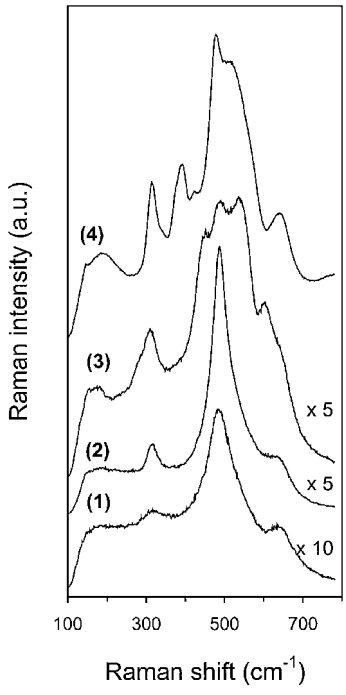

FIG. 4. Raman spectra of HSA $Ce_{0.6}Zr_{0.4}O_2$ (1), HSA $Ce_{0.6}Zr_{0.4}O_2$ calcined at 1273 K (2), REC $Ce_{0.6}Zr_{0.4}O_2$ (3), and LSA $Ce_{0.6}Zr_{0.4}O_2$ (4).

obtained for the Zr K-edge on all the samples (Table 5). The spectra were k^3-weighted and the Fourier transform was performed in the limits 3.5–14 $Å^{-1}$ using a Hanning window (see Fig. 5). In the case of the Ce L_{III}-edge the high-k part of the spectrum was limited to 8.75 $Å^{-1}$, because of the presence of the L_{II}-edge. The k^3-weighting is possible because of the high quality of our EXAFS data; this weighting is useful to enhance the metal–metal contributions in the second shell. Finally to detect any possible deviation from the appropriate stoichiometry of the Ce and Zr NNN, we allowed the Ce/Zr ratio to vary in the fitting. The aim of this procedure was to ascertain the homogeneity

TABLE 4

Results of Fitting of the EXAFS Signal at the Zr K- and Ce L_{III}-Edges: Zr and Ce NN Shell[a]

Sample	CN (Ce–O)	σ^2 (Å^2)10^{-3}	R (Å)	ΔE_0 (eV)	χ^2_ν	ν
Ce–O						
HSA	8.1 ± 0.2	9.2 ± 0.1	2.302 ± 0.003	−1.0 ± 0.1	0.362	2
REC	7.8 ± 0.2	8.3 ± 0.1	2.297 ± 0.003	−1.1 ± 0.1	1.49	2
LSA	8.7 ± 0.2	7.7 ± 0.1	2.316 ± 0.002	−0.5 ± 0.1	4.31	4
Zr–O						
HSA	5	5.9 ± 0.1	2.132 ± 0.003	3.5 ± 0.2	1.38	5
	2		2.323 ± 0.007			
REC	5	6.1 ± 0.3	2.144 ± 0.005	3.4 ± 0.2	1.49	5
	2		2.29 ± 0.01			
LSA	4	5.8 ± 0.1	2.134 ± 0.003	1.1 ± 0.2	1.36	5
	2		2.328 ± 0.008			

[a] Simulations performed with experimental standards, using EXAFS software for the Macintosh.

TABLE 5

Results of the Fitting of the EXAFS Signal at the Zr K-Edge Using *ab Initio* Calculated Parameters and Keeping CNs Fixed[a]

Shell	CN	σ^2 (Å^2)10^{-3}	R (Å^2)	ΔE_0 (eV)	χ^2_ν	ν
			HSA			
O	5	5.9 ± 0.4	2.140 ± 0.009	−6 ± 2	1.52	9
O	2		2.30 ± 0.02	−6 ± 2		
Ce	7.2	12 ± 1	3.74 ± 0.02	−8 ± 3		
Zr	4.8	15 ± 4	3.74 ± 0.02	−3 ± 4		
O	24	28 ± 6	4.32 ± 0.01	−6 ± 2		
			REC			
O	5	7 ± 1	2.16 ± 0.01	−3 ± 2	6.56	6
O	2		2.30 ± 0.04	−3 ± 2		
Ce	7.2	7.8 ± 0.8	3.75 ± 0.01	−7 ± 2		
Zr	4.8	12 ± 3	3.76 ± 0.06	3 ± 8		
O	24	17 ± 5	4.40 ± 0.03	−3 ± 2		
			LSA			
O	4	5.6 ± 0.7	2.14 ± 0.01	−1 ± 2	4.08	8
O	2		2.30 ± 0.02	−1 ± 2		
Ce	7.2	6 ± 1	3.74 ± 0.02	−5 ± 2		
Zr	4.8	7 ± 2	3.74 ± 0.05	1 ± 8		
O	24	18 ± 5	4.38 ± 0.03	−1 ± 2		

[a] Coordination numbers are fixed in the fitting of the data (compare text).

of the mixed oxide, which has often been a point of debate. The results are reported in Table 6. The analysis of the first shell in the EXFAS signal at the Ce L_{III}-edge was carried out as outlined above for the first shell of the Zr K-edge, except for allowing the coordination numbers (CNs) to fluctuate in the fitting. The results are reported in Table 4.

TABLE 6

Results of the Fitting of the EXAFS Signal at the Zr K Edge Using *ab Initio* Calculated Parameters and Allowing the Ce/Zr Ratio to Vary[a]

Shell	CN	σ^2 (Å^2)10^{-3}	R (Å)	ΔE_0 (eV)	χ^2_ν	ν
			HSA			
O	5	5.3 ± 0.4	2.14 ± 0.01	−6 ± 2	1.62	6
O	2		2.29 ± 0.02	−6 ± 2		
Ce	6 ± 4	11 ± 2	3.74 ± 0.02	−8 ± 4		
Zr	6 ± 4	17 ± 11	(3.74 ± 0.02)	−4 ± 7		
O	24	33 ± 21	4.28 ± 0.15	−6 ± 2		
			REC			
O	5	6 ± 1	2.16 ± 0.02	−3 ± 3	11.08	5
O	2		2.30 ± 0.05	−3 ± 3		
Ce	9 ± 1	7 ± 4	3.70 ± 0.04	−11 ± 4		
Zr	3 ± 1	4 ± 3	3.70 ± 0.05	−1 ± 6		
O	24	15 ± 4	4.40 ± 0.03	−3 ± 3		
			LSA			
O	4	5.1 ± 0.7	2.13 ± 0.02	−2 ± 2	4.75	7
O	2		2.29 ± 0.04	−2 ± 2		
Ce	7.9 ± 0.3	4 ± 1	3.73 ± 0.02	−6 ± 3		
Zr	4.1 ± 0.3	2 ± 2	3.74 ± 0.03	3 ± 4		
O	24	15 ± 3	4.37 ± 0.03	−2 ± 2		

[a] Ce and Zr coordination numbers were allowed to vary, keeping the sum equal to 12.

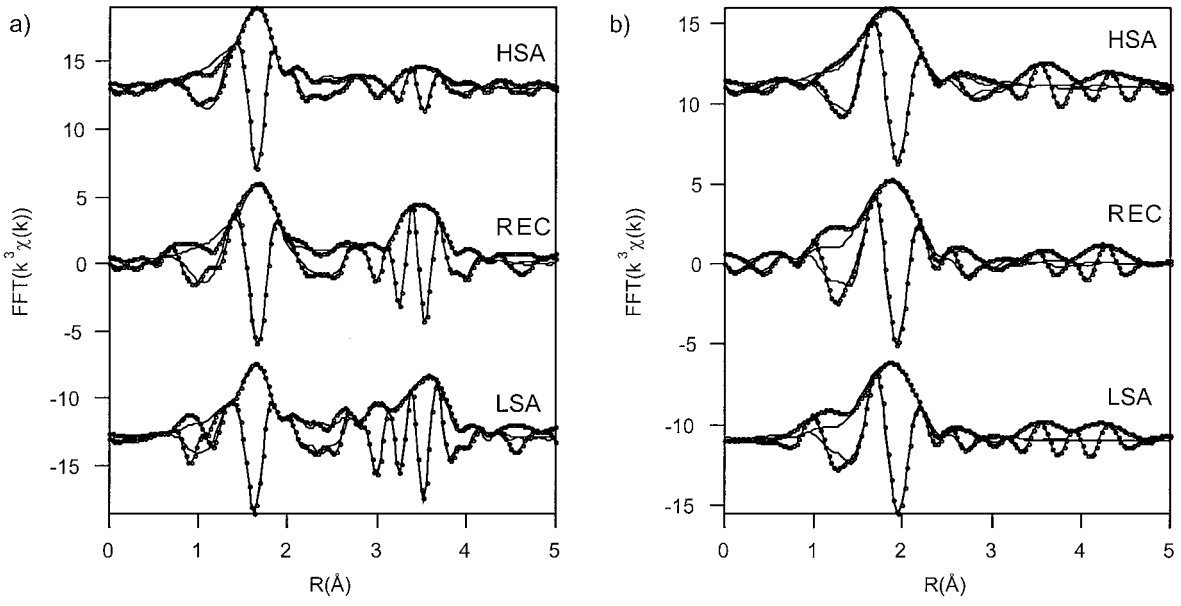

FIG. 5. (a) FFT of Zr K-edge k^3-weighted EXAFS signals; (b) FFT of Ce L_{III}-edge k^3-weighted EXAFS signals; (···) experimental signals, (—) simulations.

3.3.1. Ce L_{III}-edge. Let us first examine the results reported in Table 4 for the Ce L_{III}-edge. A perusal of the data obtained for the Ce first shell shows that CN is close to 8 in all three samples, as it occurs in the undoped CeO_2 lattice. We have tested also the 4 + 4 model for the Ce–O shell; however, due to the short k-space interval (see below) this model is indistinguishable from the single-shell model. Observation of a CN close to 8 is in agreement with the results of our previous work on LSA ceramic-type samples with a wide range of compositions (20–80% of CeO_2) where similar situation was found (6). The σ^2 value decreases along the series: HSA, REC, and LSA. It is shown below that this trend is common to σ^2 of any absorber–scatterer pair. No data are reported here on the outer shells at the Ce L_{III}-edge. In fact, obtaining information on the Ce–Ce, Ce–Zr and Ce–O NNN shells requires a large k-range. As can be seen in Fig. 6 for the K-edge of zirconium, the k^3-weighted contributions from Zr–Ce and Zr–Zr shells are dominant in a wide region around $k = 8$ Å^{-1}. If we limit our analysis to the region 3–8 Å^{-1}, a large part of the metal contribution is lost, and then the destructive interference between Zr–Ce and Zr–Zr contributions is decisive in erasing this information. A similar situation is found at the Ce L_{III}-edge, but we cannot use a large k-interval in this case. Most likely this is the reason that the FFT peaks relative to the metal–metal contributions are almost negligible. Even using the complex procedure described in Ref. (26), no satisfactory set of data for outer shells could be obtained. In agreement a similar analysis of a $Ce_{0.2}Zr_{0.8}O_2$ sample (data not reported), in which destructive interference is less important, gave satisfactory results. Further work at the K-edge of Ce is necessary to obtain detailed EXAFS information on the coordination shells of these samples.

3.3.2. Zr K-edge. The data for the Zr–O shell are reported in Table 4. In agreement with previous investigations (5, 6), the coordination around the zirconium is different from that of a fluorite-type lattice. In all the samples

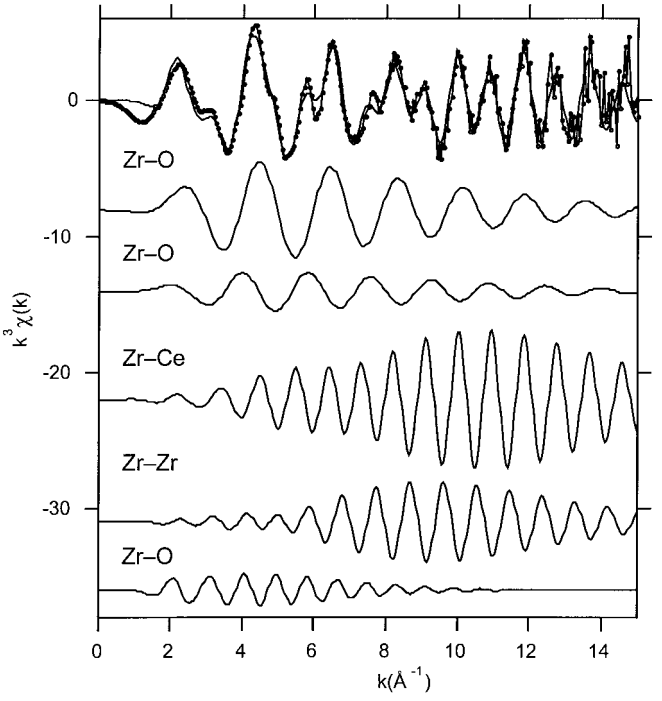

FIG. 6. (Top) Zr K-edge k^3-weighted EXAFS signals of the LSA sample (···) and its simulation (—); single contributions to the total signal are shown; note that the phase opposition of Zr–Ce and Zr–Zr contributions partially erases second shell signal.

investigated, a single shell CN = 8 did not fit the data. Only two subshell models properly fit the EXAFS signal. Remarkably, we found that HSA, REC, and LSA samples show different levels of coordination around zirconium. Notice that the 5 + 2 and 4 + 2 models are different, even if the absolute values of these numbers can suffer a loss of approximately 10% in accuracy. This is a strong indication that, despite the same sample composition, structural properties differ according to the sample origin.

Lack of detection of eight oxygen atoms around the Zr cation is attributed to the structural disorder of the oxygen sublattice. Apparently the relatively small Zr is not able to accommodate eight oxygen atoms in its coordination sphere in a similar fashion to the Ce cation, favoring a displacement of the undetected oxygen atoms to a distance further than the length of the first Zr coordination shell. The value of σ^2 is similar in all compounds and the differences are less than the error bar.

It is important to notice the good agreement between the data for the NN Zr–O shell as reported in Table 4 and the corresponding data reported in Table 5. Keeping in mind that different procedures were adopted in these analyses, the consistency of the results strongly supports the validity of the present model.

The analysis of the Zr second shell discloses some interesting features. For the NNNs of zirconia, the main target of the analysis was the detection of the presence or absence of a homogeneous solid solution. In fact, due to the metastable nature of the CeO_2–ZrO_2 mixed oxides of intermediate composition, the possibility of forming a truly homogeneous solid solution has often been questioned. Also redox cycling and thermal aging could themselves induce a phase separation as has recently been observed under oxidizing conditions for some CeO_2–ZrO_2 mixed oxides of similar compositions (15). For this purpose we carried out the analysis both by keeping the Zr–Zr and Zr–Ce at the stoichiometric values (Table 5) and by varying the ratio Zr/Ce (Table 6). In all cases building a model using the hypothesis of a solid solution and a cubic cation-sublattice leads to fairly good simulation of the Fourier signal up to 4.1 Å (compare Fig. 6 and Table 5). In contrast, leaving the Ce/Zr ratio free to vary (Table 6), we obtain an increase of the χ^2_ν parameter. This indicates that this procedure does not improve the quality of the fitting; furthermore, the Ce/Zr ratio obtained has a large error bar, particularly for the HSA sample, while the value is near the stoichiometric composition. Notice that in the case of the REC sample the value obtained is unreliable, since it would indicate that the Zr second shell has been enriched in Ce content. Keeping in mind that we are investigating the sample at the Zr K-edge, phase separation should lead to an increase of Zr NNN since Zr- and Ce-rich phases would be formed in this process. Finally, the value obtained for the LSA sample does not change significantly compared to the model reported in Table 5. We can therefore conclude that within the limits of the sensitivity of this technique we do not have evidence for the occurrence of an appreciable phase separation, either for the fresh or for the REC/LSA sample.

There is a general observation concerning the Debye–Waller factors: they rapidly decrease along the series HSA, REC, and LSA, while the average distances Zr–Zr, Zr–Ce, and Zr–O remain unchanged. This suggests that the dispersion of the bonding distances may change along the series of the three samples, with the structure becoming more and more ordered. At present we do not have a clear explanation for such an observation except a suggestion that, perhaps, this effect could be related to the increase in the treatment temperature, which apparently induces some structural rearrangements in the lattice. This effect is particularly noticeable in the LSA sample.

At this point the XRD results should be recalled. In fact we observe a good agreement between the two techniques: M–M bond distances of 3.763, 3.752, and 3.753 Å were determined by XRD, which agree within 0.02 Å, i.e., within the error bar, with those found by EXAFS. Importantly, the agreement with the Ce–Zr and Zr–Zr bond distances reported in Table 4 independently confirms the validity of our approach, i.e., the use of *ab initio* calculations. As far as the Zr–O bond distances are concerned, the values obtained by XRD are close to those determined by EXAFS for both Ce–O and the second Zr–O subshell. Even if a good agreement of the profile fitting was obtained only for the HSA $Ce_{0.6}Zr_{0.4}O_2$, most likely the average M–O bond length is close to those detected in Tables 2 and 3. In fact, where the XRD fails to appropriately describe the structure, the largest distortions of the oxygen sublattice are found by EXAFS.

In summary the EXAFS data confirm the XRD and Raman observations that the structural properties of these samples are highly sensitive to the sample pretreatment and the preparation method. The different coordination numbers of the first oxygen shell and the trend of Debye–Waller factors give evidence of this fact. It is noteworthy that the oxygen sublattice is particularly dependent on the preparation method, with the LSA sample being significantly different from both the HSA and the REC samples. We believe that the contraction of the Zr–O first coordination shell leading to disordered, mobile oxygen atoms in the lattice is the main factor responsible for the easy reduction in the bulk of these mixed oxides. In this respect, the unusually low reduction temperature observed for the reduction of the Rh(LSA)/$Ce_{0.6}Zr_{0.4}O_2$ samples seems to be associated with a low coordination number compared to both HSA and REC samples. On the other hand, the relatively low Debye–Waller factors suggest that some ordering in the cationic lattice may occur, leading to an oxygen release capacity that is lower than those of the HSA and REC $Ce_{0.6}Zr_{0.4}O_2$. As far as the comparison of the

redox behavior of the HSA and REC $Ce_{0.6}Zr_{0.4}O_2$ is concerned, the structural characterization suggests that the distortions in the oxygen sublattice are more significant in the REC sample than in the HSA sample. Reduction of REC $Ce_{0.6}Zr_{0.4}O_2$ occurs, however, at a temperature that is higher than that for the HSA $Ce_{0.6}Zr_{0.4}O_2$. It appears that a rationale for this behavior must take into account a combination of different properties of the mixed oxides, including the textural ones. In fact, the surface area of HSA $Ce_{0.6}Zr_{0.4}O_2$ strongly decreases after the TPR cycle. Accordingly, recently the sensitivity of the redox behavior of the CeO_2–ZrO_2 mixed oxides to the pretreatment conditions was reported (4, 27).

4. CONCLUSIONS

The present results have disclosed significant effects of the degree of sintering and pretreatment on the CeO_2–ZrO_2 redox properties. The order/disorder of the oxygen sublattice, generated by insertion of ZrO_2 into the CeO_2 lattice, is indicated as a key factor in promoting reduction in the majority of these mixed oxides. Significant differences are found between the Zr–O bonding in materials derived from a high-surface-area mixed oxide and the sintered ceramic-type mixed oxides, as the coordination number decreases from 7 to 6. In analogy with ZrO_2, we interpret these differences in terms of dependency of the phase nature on the particle size and the precursor. In fact, the data clearly point out that remarkable differences exist among different samples of a single composition, for which the presence of the t'' phase was suggested.

ACKNOWLEDGMENTS

University of Trieste, the Ministero dell'Ambiente (Rome), contract DG 164/SCOC/97, CNR (Rome) Programmi Finalizzati "Materiali Speciali per Tecnologie Avanzate II," Contract 97.00896.34, and MURST "Programmi di Ricerca Scientifica di Rilevante Interesse Nazionale—1998" are gratefully acknowledged for financial support. The technical assistance of the staff from LURE is gratefully acknowledged.

REFERENCES

1. Pijolat, M., Prin, M., Soustelle, M., Touret, O., and Nortier, P., *J. Chem. Soc. Faraday Trans.* **91**, 3941 (1995).
2. Fornasiero, P., Di Monte, R., Ranga Rao, G., Kaspar, J., Meriani, S., Trovarelli, A., and Graziani, M., *J. Catal.* **151**, 168 (1995).
3. Fornasiero, P., Balducci, G., Di Monte, R., Kaspar, J., Sergo, V., Gubitosa, G., Ferrero, A., and Graziani, M., *J. Catal.* **164**, 173 (1996).
4. Fornasiero, P., Kaspar, J., and Graziani, M., *Appl. Catal. B Environ.* **22**, L11 (1999).
5. Vlaic, G., Fornasiero, P., Geremia, S., Kaspar, J., and Graziani, M., *J. Catal.* **168**, 386 (1997).
6. Vlaic, G., Di Monte, R., Fornasiero, P., Fonda, E., Kaspar, J., and Graziani, M., *J. Catal.* **182**, 378 (1999).
7. Ranga Rao, G., Kaspar, J., Di Monte, R., Meriani, S., and Graziani, M., *Catal. Lett.* **24**, 107 (1994).
8. Vidmar, P., Fornasiero, P., Kaspar, J., Gubitosa, G., and Graziani, M., *J. Catal.* **171**, 160 (1997).
9. Rehr, J. J., Booth, C. H., Bridges, F., and Zabinsky, S. I., *Phys. Rev. B* **49**, 12347 (1994).
10. Fornasiero, P., Kaspar, J., and Graziani, M., *J. Catal.* **167**, 576 (1997).
11. Fornasiero, P., Kaspar, J., Sergo, V., and Graziani, M., *J. Catal.* **182**, 56 (1999).
12. Yashima, M., Arashi, H., Kakihana, M., and Yoshimura, M., *J. Am. Ceram. Soc.* **77**, 1067 (1994).
13. Kaspar, J., Fornasiero, P., and Graziani, M., *Catal. Today* **50**, 285 (1999).
14. Tani, E., Yoshimura, M., and Somiya, S., *J. Am. Ceram. Soc.* **66**, 506 (1983).
15. Colon, G., Pijolat, M., Valdivieso, F., Vidal, H., Kaspar, J., Finocchio, E., Daturi, M., Binet, C., Lavalley, J. C., Baker, R. T., and Bernal, S., *J. Chem. Soc. Faraday Trans.* **94**, 3717 (1998).
16. Leonov, A. I., Andreeva, A. B., and Keler, E. K., *Izv. Akad. Nauk SSSR Neorg. Mater.* **2**, 137 (1966).
17. Yashima, M., Hirose, T., Kakihana, M., Suzuki, Y., and Yoshimura, M., *J Am. Ceram. Soc.* **80**, 171 (1997).
18. Yashima, M., Ohtake, K., Arashi, H., Kakihana, M., and Yoshimura, M., *J. Appl. Phys.* **74**, 7603 (1993).
19. Keramidas, V. G., and White, W. B., *J. Am. Ceram. Soc.* **57**, 22 (1974).
20. McBride, J. R., Hass, K. C., Poindexter, B. D., and Weber, W. H., *J. Appl. Phys.* **76**, 2435 (1994).
21. Graham, G. W., Weber, W. H., Peters, C. R., and Usmen, R. K., *J. Catal.* **130**, 310 (1991).
22. Yashima, M., Ohtake, K., Kakihana, M., Arashi, H., and Yoshimura, M., *J. Phys. Chem. Solids* **57**, 17 (1996).
23. Yashima, M., Morimoto, K., Ishizawa, N., and Yoshimura, M., *J. Am. Ceram. Soc.* **76**, 1745 (1993).
24. Michalowicz, A., "Logiciel pour la Chimie," p. 751, Societé Francaise de Chimie, Paris, 1991.
25. Stern, E. A., Newville, M., Ravel, B., Yacoby, Y., and Haskel, D., *Physica B* **208/209**, 117 (1995).
26. Fonda, E., Andreatta, A., Colavita, P. E., and Vlaic, G., *J. Synchr. Rad.* **6**, 34 (1999).
27. Baker, R. T., Bernal, S., Blanco, G., Cordon, A. M., Pintado, J. M., Rodriguez-Izquierdo, J. M., Fally, F., and Perrichon, V., *Chem. Commun.*, 149 (1999).